

# CAMLD: Contrast-Agnostic Medical Landmark Detection with Consistency-Based Regularization

Soorena Salari<sup>1\*</sup>Arash Harirpoush<sup>1</sup>Hassan Rivaz<sup>2</sup>Yiming Xiao<sup>1</sup><sup>1</sup>Department of Computer Science and Software Engineering, Concordia University, Montréal, Canada<sup>2</sup>Department of Electrical and Computer Engineering, Concordia University, Montréal, Canada

## Abstract

Anatomical landmark detection in medical images is essential for various clinical and research applications, including disease diagnosis and surgical planning. However, manual landmark annotation is time-consuming and requires significant expertise. Existing deep learning (DL) methods often require large amounts of well-annotated data, which are costly to acquire. In this paper, we introduce **CAMLD**, a novel self-supervised DL framework for anatomical landmark detection in unlabeled scans with varying contrasts by using only a single reference example. To achieve this, we employed an inter-subject landmark consistency loss with an image registration loss while introducing a 3D convolution-based contrast augmentation strategy to promote model generalization to new contrasts. Additionally, we utilize an adaptive mixed loss function to schedule the contributions of different sub-tasks for optimal outcomes. We demonstrate the proposed method with the intricate task of MRI-based 3D brain landmark detection. With comprehensive experiments on four diverse clinical and public datasets, including both T1w and T2w MRI scans at different MRI field strengths, we demonstrate that **CAMLD** outperforms the state-of-the-art methods in terms of mean radial errors (MREs) and success detection rates (SDRs). Our framework provides a robust and accurate solution for anatomical landmark detection, reducing the need for extensively annotated datasets and generalizing well across different imaging contrasts. Our code will be publicly available at <https://github.com/HealthX-Lab/CAMLD>.

## 1. Introduction

Anatomical landmarks in medical images are salient key-points with clinical significance in bodily structures, such as the knee [21], spine [59], and lungs [50]. They often serve as essential reference points to facilitate anatomical

navigation and measurement of physiological changes for diagnostic purposes and surgical planning. With an aging global population, neurological disorders are becoming increasingly prominent issues. With a long history in neurological research and patient care, brain landmarks as shown in MRI are of great interest to the clinical and research communities, but are more complex due to the intricate neuroanatomy, softer geometric features (compared to bones), and high precision requirement in deployment. Besides the traditional task of anatomical localization for planning functional neurosurgery [56], brain landmarks [46, 63] have also been employed to diagnose neurodegenerative conditions, such as Parkinson’s disease [1] and Alzheimer’s disease [62]. Additionally, for big data analysis of brain MRIs, where subject-to-template image registration is crucial, brain landmarks can provide the essential tool to assess the quality of image alignment to ensure the reliability of the study. Notably, thanks to their high spatial specificity, brain landmarks can offer better sensitivity and interpretability in registration quality assessment than other volume-overlap-based metrics (e.g., Dice coefficient) [37]. However, manual landmark annotation requires significant domain expertise, time, and labor. Thus, automated anatomical landmark detection is highly instrumental.

With state-of-the-art (SOTA) performance across a wide range of complex medical image processing tasks, deep learning (DL)-based algorithms have emerged as the dominant approaches for accurate and effective anatomical landmark detection [12, 28, 63]. So far, relevant studies primarily focus on using convolutional neural networks (CNNs) to extract relevant image features to locate target landmarks, [28, 39, 66], as either fuzzy heatmaps [48] or regressed coordinates [39]. With privacy concerns and difficulty in acquiring expert annotations, few public datasets for anatomical landmark detection with clinical protocols exist, posing major barriers to the development and validation of relevant DL-based methods, especially for supervised approaches.

Lately, label-efficient methods, such as one-shot [67] and few-shot learning [34, 35] have gained great interest to alleviate the need for large-scale annotations, by giv-

\*Correspondence to: soorena.salari@concordia.ca.

ing limited exemplary prototypes during inference. To push the boundary further, recent studies have adopted self-supervised learning (SSL) strategies for efficient representation learning to generate anatomical landmarks, by training keypoint-based image registration models [5, 6, 16, 52, 53]. However, the allocation of the learned landmarks from these models can be random because no explicit expert knowledge is involved in the SSL setup, where image registration loss provides the sole guidance in feature learning. As clinical landmarks require a consistent localization protocol for each keypoint’s anatomical context, which often has an overlap in geometric saliency and anatomical/physiological significance, the landmarks obtained from these SSL models may not serve well in clinical applications. As a result, alternative effective SSL approaches to obtain clinically meaningful anatomical landmarks still require further investigation. Despite their limitations, these recent works [5, 6, 10, 16, 52, 53] demonstrated that image registration and anatomical landmark localization learning are two tasks with a strong synergy. Compared with prior relevant CNN works [12, 22] that rely on popular hierarchical strategies to better understand the spatial context of landmark sets in a coarse-to-fine manner, such duality may offer a more elegant and efficient solution for accurate landmark tagging. Thus, we expect that a multi-task learning strategy, which carefully considers the balance of the learning schedules for these two tasks [9, 25] could bring benefits for our goal. In addition, sensitivity to scanner types, scanning parameters, and image contrasts has been a well-known issue in DL-based medical image analysis. Besides regular Gamma-correction-based contrast augmentation, existing landmark detection techniques have attempted to mitigate this issue by adopting computationally expensive metrics, such as Mutual Information (MI) and Modality Independent Neighborhood Descriptor (MIND) [6] and incorporating additional loss functions to enforce cross-contrast consistency [52]. However, these measures still require real multi-contrast datasets during training, which could be difficult depending on the task domain. Alternatively, besides contrast synthesis using anatomical segmentation maps [19], which may not be readily available and may struggle to capture nuanced details in scans, more flexible and drastic contrast alteration based on CNN [33, 42, 55] may offer the needed benefits. While this method has been adopted in 2D medical image analysis, it is yet to be adapted for volumetric data for landmark feature learning.

In general, there are three main challenges in DL-based medical landmark detection. **First**, the reliance on manual annotations is both time-intensive and prone to rater variability, limiting the availability of high-quality labeled datasets for algorithm development and validation. **Second**, existing methods often struggle to generalize across different imaging contrasts or modalities, requiring costly

multi-contrast/modal datasets or extensive domain-specific retraining. **Finally**, existing self-supervised approaches often produce landmarks that lack anatomical consistency, as they focus on optimizing registration similarity metrics rather than ensuring consistent alignment with anatomically significant regions. To address these limitations of previous works, we present a novel self-supervised DL framework, called **CAMLD** that employs multi-task learning for contrast-agnostic anatomical landmark detection. With unbiased representation of anatomical features, population-averaged anatomical atlases made from medical scans of a large cohort [57] are often used as the reference for spatial normalization and anatomical navigation in clinical tasks. Besides typically providing the definition of anatomical segmentation, we hypothesize that they can also provide the means to inject needed expert knowledge into an annotation-efficient SSL framework for landmark detection. We demonstrate our method for the challenging task of 3D brain landmark detection in multi-contrast MRIs, which have been largely under-explored despite the great demand.

The major contributions of this paper are as follows:

- We introduce an innovative and data-efficient self-supervised framework for anatomical landmark detection by leveraging inter-scan landmark consistency to enforce a systematic landmark protocol across subjects, with the requirement of only a single reference atlas annotation.
- To enable model generalization to unseen MRI contrasts, we propose an effective 3D contrast augmentation strategy using random convolution without the need for real multi-contrast training data.
- We propose an adaptive mixed loss function, inspired by curriculum learning to dynamically balance registration similarity and landmark consistency for robust anatomical feature learning.
- We conduct comprehensive validation on the proposed method using four diverse clinical and public datasets at different MR field strengths. The results demonstrate the efficacy of the proposed components, achieving significant performance improvements over SOTA approaches.

## 2. Related Work

### 2.1. Landmark Transfer via Atlas Propagation

Classical atlas-to-subject registration methods (e.g., ANTs [3] and NiftyReg [29]) are foundational approaches for anatomical landmark detection, relying on the calculation of deformation vector fields (DVF) to warp landmarks from the atlas space to the subject space. While effective for global alignment, these methods are slow, computationally expensive, and often fail to capture fine-grained anatomical details, limiting their utility in time-sensitive and precision-

critical applications. Although more recent DL-based registration can significantly enhance inference speed, classic methods still set the bar for accuracy [11] and atlas-propagation-based landmarks are sub-optimal for registration quality assessment due to the inherent bias towards the source registration method.

## 2.2. Supervised Landmark Detection

Supervised DL methods for landmark detection have dominated the literature, by generating heat maps [28] or regressing the position coordinates of the predicted keypoints [24, 63]. To reduce the computational cost of these models for 3D images, some works also reformat the task into 2.5D feature extraction instead [61]. Multi-stage techniques, such as 3D Faster R-CNN [12] and Mask R-CNN [22] identify landmarks within initially localized target regions in a coarse-to-fine paradigm. Also, U-Net architectures, combined with attention mechanisms, have been frequently employed to improve the accuracy of anatomical landmark detection [23, 24]. Nevertheless, the primary bottleneck of supervised landmark detection is the poor availability of annotated landmarks, motivating novel SSL frameworks to tackle such challenges.

## 2.3. Self-Supervised Landmark Detection

Recently, SSL has gained interests in anatomical landmark detection. Chao et al. [10] propose a framework that discovers anatomically consistent landmarks between scans by combining a landmark discovery loss with a deformation reconstruction loss, leveraging an external registration model to ensure accurate correspondences. However, the accuracy of their method can heavily depend on the chosen registration model, with potential model biases and limited adaptability to unseen contrasts. Medical image registration frameworks that leverage keypoint alignment between scans have also been explored for landmark discovery to help visually explain DL-based registration outcomes [5, 6, 52, 52, 53]. These techniques extract landmarks from two subjects and subsequently estimate the DVFs. However, as the main objective of these methods is image registration, with the primary guidance of conventional similarity losses, such as MSE and MIND (along with DVFs smoothness constraints), the “discovered” landmark pairs are often located in regions that are strategic for image alignment and vary among inference samples. Thus, it is not ideal for generating clinical anatomical landmarks, which follow consistent protocols across subjects and image contrasts. Finally, to enable adaptability to different image contrasts, Wang et al. [52] presented a self-supervised loss to enforce consistency between predicted landmarks for the same subject’s multi-contrast scans. However, the limited multi-contrast/modal datasets can pose difficulty for this approach.

## 2.4. Multi-task Learning

Multi-task learning is often employed for landmark detection tasks by associating landmark detection with other downstream tasks, such as image classification, image segmentation, and reconstruction [20, 49, 64]. Browatzk et al. [9] employed supervised transfer learning based on facial image reconstruction for landmark detection. Lian et al. [25] introduced a dynamic multi-task Transformer network to detect dental landmarks together with bone segmentation. In our study, we couple the tasks of landmark detection with image registration. Unlike other multi-task learning methods that share feature embeddings, our framework uses image registration to assist the model in initializing the landmarks, after which our consistency regularization terms calibrate the detected landmarks. A curriculum learning approach [4, 54] is also employed to mitigate the interferences between the two tasks.

## 3. Materials and Methods

### 3.1. Problem Setup and Overview

Let  $\mathbf{X} = \{x_i \subseteq \mathbb{R}^N\}_{i=1, \dots, K}$  be the training set of  $K$  unlabeled volumetric scans. Additionally, we used a single template image,  $I_{\text{template}} \subseteq \mathbb{R}^N$  that contains  $L$  expert-annotated landmarks,  $\mathbf{P} = \{P_n \in \mathbb{R}^3\}_{n=1, \dots, L}$ . Given the training scans and a single template with annotated landmarks, our objective is to optimize the anatomical landmark detection model  $\mathbf{f}(\cdot; \theta)$  to accurately detect the corresponding anatomical landmarks that are defined in the single template in the other scans.

Figure. 1 provides an overview of our proposed framework. We begin by randomly selecting  $M$  volumetric scans from the training set  $\mathbf{X}$ . These scans undergo contrast and geometric augmentations before being processed by the landmark detection model  $\mathbf{f}(\cdot; \theta)$ , which predicts the anatomical landmarks. For each scan, transformations are then computed based on the template landmarks  $\mathbf{P}$  and the predicted landmarks, aligning the volumetric scan and predicted landmarks to the template space. Finally, two distinct loss functions are calculated to train the model effectively.

### 3.2. Training Loss

Let  $\mathbf{X}_M = \{x_{i_1}, x_{i_2}, \dots, x_{i_M}\}$ , where  $\{i_1, i_2, \dots, i_M\} \subset \{1, \dots, K\}$ , be  $M$  random samples from the whole  $K$  samples in the training set. Also,  $T_\beta$  denotes the analytical and differentiable deformation field with control parameters  $\beta$ , as presented in the *Supplementary Materials*.

For all images  $x_i \in \mathbf{X}_M$ , we obtain  $L$  anatomical landmarks:  $\{\mathbf{f}(x_{i_1}; \theta), \mathbf{f}(x_{i_2}; \theta), \dots, \mathbf{f}(x_{i_M}; \theta)\}$ . Subsequently,  $M$  deformation fields were obtained:  $\{T_{\beta_{i_1}^*}, \dots, T_{\beta_{i_M}^*}\}$ , where  $\beta^* = G(\mathbf{P}, \mathbf{f}(x_i; \theta))$  and  $G$  is the function to calculate the parameter  $\beta^*$  based on the pairs of template and predicted landmarks ( $\mathbf{P}$  vs.  $\mathbf{f}(x_i; \theta)$ )

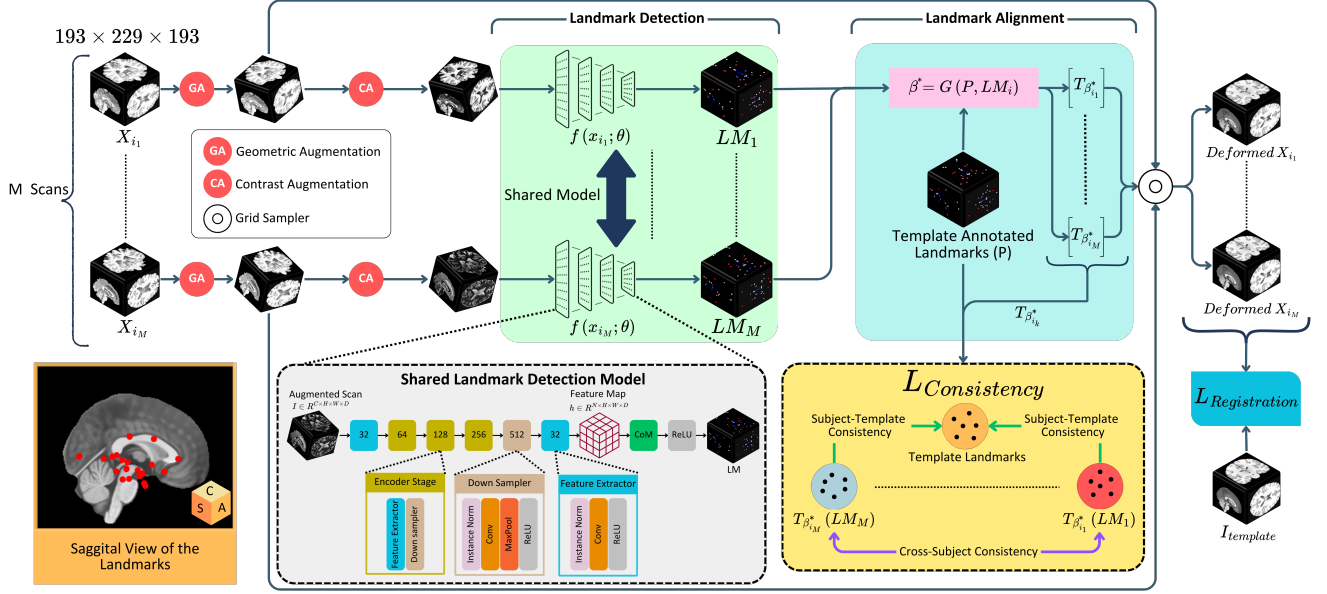


Figure 1. Overview of the proposed framework and the consistency-based learning approach. For simplicity, 3D scans are presented in a 2D perspective for visualization.

and the pre-determined spatial transformation model. The interpolation requirements can be relaxed (e.g., to handle noise) by incorporating a regularization term  $\lambda > 0$ :

$$G(\mathbf{P}, \mathbf{f}(x_i; \theta)) = \arg \min_{\beta} \sum_{j=1}^L (T_{\beta}(\mathbf{f}(x_i; \theta))^{(j)} - \mathbf{P}^{(j)})^2 + \lambda I, \quad (1)$$

where  $\lambda$  is a hyperparameter that determines the level of regularization. For the thin-plate splines (TPS) transformation model, when  $\lambda \rightarrow \infty$ , the optimal transformation tends to be an affine transformation (i.e., zero bending energy). During the training process, this parameter can be drawn from a distribution  $\lambda \sim N(\lambda)$ , learning both affine and non-linear transformations.

**Registration Loss:** The registration loss function,  $\mathcal{L}_{\text{registration}}$  of our training to align the subject's scan ( $x_{i_k}$ ) to the template image ( $I_{\text{template}}$ ) is defined as:

$$\mathcal{L}_{\text{registration}} = \frac{1}{M} \sum_{k=1}^M \mathcal{L}_{\text{sim}}(x_{i_k} \circ T_{\beta_{i_k}^*}, I_{\text{template}}), \quad (2)$$

where  $\mathcal{L}_{\text{sim}}$  and  $\circ$  denote similarity loss function and spatial transformation operation, respectively.

**Consistency Loss:** To regularize the landmark predictions across the training samples, we include the cross-subject landmark position consistency loss  $\mathcal{L}_{\text{consistency}_1}$  and the subject-template counterpart  $\mathcal{L}_{\text{consistency}_2}$ :

$$\mathcal{L}_{\text{consistency}_1} = \frac{1}{\binom{M}{2}} \sum_{1 \leq r < j \leq M} \left\| T_{\beta_{i_r}^*}(\mathbf{f}(x_{i_r}; \theta)) - T_{\beta_{i_j}^*}(\mathbf{f}(x_{i_j}; \theta)) \right\|_2, \quad (3)$$

$$\mathcal{L}_{\text{consistency}_2} = \frac{1}{M} \sum_{k=1}^M \left\| T_{\beta_{i_k}^*}(\mathbf{f}(x_{i_k}; \theta)) - \mathbf{P} \right\|_2, \quad (4)$$

$$\mathcal{L}_{\text{consistency}} = \mathcal{L}_{\text{consistency}_1} + \mathcal{L}_{\text{consistency}_2}, \quad (5)$$

As clinical anatomical landmarks typically follow a pre-defined protocol, this requires inter-subject consistency in point placement regardless of individual anatomical variations. We hypothesize that  $\mathcal{L}_{\text{consistency}_1}$  should reinforce this requirement while  $\mathcal{L}_{\text{consistency}_2}$  ensures the consistency of the predicted landmark protocol with the reference template.

**Total Training Loss:** The total training loss for our framework is defined as:

$$\mathcal{L}_{\text{total}} = (1 - \alpha) \mathcal{L}_{\text{registration}} + \alpha \mathcal{L}_{\text{consistency}}, \quad (6)$$

In multi-task learning, sub-task interference is a common challenge [60]. In our case, there is an observed interference between the landmark prediction and registration tasks. To address this issue, we build on insights from prior research [31, 32, 41, 54] and introduce the parameter  $\alpha$  to balance objectives and guide the optimizer more effectively. We define  $\alpha$  as follows:

$$\alpha = \frac{2}{1 + \exp(-5\eta)} - 1, \quad (7)$$

where

$$\eta = \frac{\text{current training iteration}}{\text{total training iterations}}, \quad (8)$$

During training, the growing  $\alpha$  is linked to the ratio  $\eta$ , which tracks the completion progress of training iterations. This allows the optimizer to initially emphasize  $\mathcal{L}_{\text{registration}}$  for the registration task to gain an understanding of anatomical features, and then shift the focus toward refining anatomical landmark predictions. This approach resembles curriculum learning [4, 54], and reduces convergence risk to local minima in the early epochs, promoting more accurate and robust learning.

### 3.3. Anatomical Landmark Detection Model

We utilized a 3D CNN for landmark detection, consisting of nine convolutional blocks, each incorporating 3D convolutional layers, instance normalization, ReLU activations, and max pooling for feature downsampling. The filter count starts at 32 and increases progressively to 512, capturing features at multiple scales. In the final block, the feature channels are reduced to 32, enabling compact yet informative representations. The network processes the input image  $I \in \mathbb{R}^{C \times H \times W \times D}$  and produces a feature map  $h \in \mathbb{R}^{N \times H \times W \times D}$ , where  $C$  is the number of input channels, and  $H$ ,  $W$ , and  $D$  represent the height, width, and depth of the scan, respectively, while  $N$  is the number of output feature maps. Rather than producing a single output, this network architecture generates multiple feature maps in the final layer, each representing a specific anatomical landmark. These feature maps are then passed through a center of mass (CoM) layer [26, 44], which computes the center of mass for each feature map and predicted landmark coordinates. The full network architecture is depicted at the bottom of the Figure. 1.

### 3.4. Contrast and Geometric Augmentation

To develop a contrast-agnostic registration framework, we introduce a method that emulates a wide range of image contrasts using random convolution (RC) [58] for contrast augmentation in 3D radiological tasks for the first time. RC has been beneficial in creating robust representations for domain generalization across both computer vision and medical imaging tasks in 2D, such as segmentation and classification [33, 42, 55]. This technique utilizes randomly initialized convolutional filters to modify the visual characteristics of input images while preserving their geometric and structural integrity. Previous research indicates that using large kernels in RC can lead to blurring, which can be problematic for registration tasks that depend on detailed image features to establish pixel-level correspondences. To address

this issue, we employ a  $1 \times 1 \times 1$  kernel size to minimize artifacts and retain structural details. To cover a broad range of contrast variations, we sequence a set of RC layers with LeakyReLU activation, enabling the network to model complex, non-linear intensity relationships among various MRI contrasts. The convolutional kernel parameters in each RC layer are independently drawn from uniform distributions, ensuring a broad range of contrast transformations. RC enables the network to learn landmarks in a contrast-invariant manner, helping to improve the generalization and stabilize the training process. Samples of contrast augmented scans with RC are shown in the *Supplementary Materials*. Moreover, we performed random affine augmentations on the scans as our geometric augmentation during training. This augmentation ensures that the model learns to detect landmarks accurately, even under varying spatial configurations, improving generalization to unseen data.

## 4. Experiments

### 4.1. Data and Pre-Processing

**Training data:** For the reference template ( $I_{\text{template}}$ ), we used the widely adopted T1w ICBM152-MNI2009c Symmetric brain MRI template [17], along with 32 expert-annotated landmarks ( $\mathcal{P}$ ) based on the AFIDS protocol [46]. Although other landmark protocols also exist, we have chosen this protocol due to its clinical significance and public accessibility of the relevant data. To train our model, we have curated multi-center datasets of balanced sexes and ages (18-90 yo) to build our training set. For our training set, we obtained 1544 brain MRI datasets (3T & 7T) by combining 581 T1w brain MRIs from the IXI dataset<sup>1</sup>, 105 7T T1w brain MRIs from the AHEAD dataset [2], 634 T1w brain MRIs from the HCP-A dataset [51], and 224 T1w brain MRIs from OpenNeuro [40, 45]. We conduct standard pre-processing for all scans: resizing and resampling to  $193 \times 229 \times 193$  voxels and  $1 \times 1 \times 1 \text{ mm}^3$  resolution, rescaling intensity values to [0, 1], skull-stripping using BEaST [15], applying an N4 bias field correction, and affine registration to the ICBM152 space [18].

**Testing data:** To evaluate the effectiveness of our method, we have utilized 122 scans from 4 different sources: 1) 30 T1w MRI scans from the HCP dataset [51] acquired on a 3T scanner, 2) 30 T1w MRI scans from the publicly available Open Access Series of Imaging Studies (OASIS-1) [27] database acquired on a 3T scanner, 3) 32 T1w MRI scans from the Stereotactic Neurosurgery (SNSX) dataset [46] acquired on a 7T scanner, and 4) 30 T2w MRI scans from the HCP dataset. For each scan, 32 AFIDS landmarks [46] were manually labeled by experts, consistent with the template we utilized in training.

<sup>1</sup><https://brain-development.org/ixi-dataset>

## 4.2. Implementation

All learning-based methods were implemented using PyTorch. We utilized the Adam optimizer with an initial learning rate of  $10^{-4}$  and a cosine annealing scheduler with a minimum learning rate of  $10^{-6}$ . To balance computational efficiency,  $M$  was set to 2. The model was trained for 2500 epochs. Also, we used TPS as our deformation field ( $T_\beta$ ) model and mean-squared error (MSE) as similarity loss function ( $\mathcal{L}_{\text{sim}}$ ). For TPS, the regularization parameter ( $\lambda$ ) was randomly sampled from a log-uniform distribution ranging between 0 and 10. For random affine augmentation, the parameters are uniformly sampled as follows: rotations within  $[-180^\circ, +180^\circ]$ , translations between  $[-15, 15]$  voxels, scaling factors in  $[0.8, 1.2]$ , and shear values in the interval  $[-0.1, 0.1]$ . Lastly, the RC-based contrast augmentation includes five RC layers, each with kernel weights drawn from a random uniform distribution  $U(0, 2)$ . After sampling, these kernel weights are adjusted to be zero-centered. Each RC layer is followed by a LeakyReLU activation function with a negative slope of 0.2.

## 4.3. Evaluation Metrics and Baselines

To assess the effectiveness of our framework, we employed mean radial error (MRE) and success detection rate (SDR). MRE calculates the average Euclidean distance between predictions ( $y$ ) and ground truths ( $\hat{y}$ ). SDR measures the percentage of predictions within a predefined threshold  $\tau$  from the ground truths, given by  $SDR_\tau = \frac{1}{S \times L} \sum_{j=1}^S \sum_{i=1}^L \mathbf{1}(\|y_j^i - \hat{y}_j^i\|_2 < \tau) \times 100\%$ , where the indicator function  $\mathbf{1}(\cdot)$  returns 1 if the Euclidean distance between  $y$  and  $\hat{y}$  is less than  $\tau$ , and 0 otherwise and  $S$  and  $L$  are representing the number of test scans and number of landmarks in each scan, respectively. For these metrics, lower MRE values indicate higher positional accuracy, while higher SDR values reflect a greater proportion of predictions within the acceptable threshold, both signaling improved model performance. Furthermore, we evaluated statistical significance using paired t-tests to compare the performance of our method against baseline methods. A  $p$ -value less than 0.05 indicates statistical significance.

We compare our method against three classic SOTA traditional methods (ANTs [3], NiftyReg [29], and 3D SIFT [36]), four SOTA learning-based approaches (KeyMorph [52], BrainMorph [53], uniGradICON [47], MultiGradICON [13]), and one fully supervised CNN. For ANTs, we implemented two versions: one using the MI metric and the other using the cross-correlation (CC) metric, both with a multi-resolution approach (10x50x50x20) and SyN (Symmetric Normalization) transformation with a gradient step size of 0.25. For NiftyReg, we employed its non-rigid registration algorithm with the normalized mutual information (NMI) metric. In all registration algorithms, the deformation fields from template-to-subject registration were ap-

plied to warp the landmarks from the template space to the subject space for prediction calculation. For 3D SIFT, we used SIFT features in the template space to locate corresponding landmarks in the subject space by identifying the closest match with cosine similarity across 3D SIFT points. For KeyMorph [52], BrainMorph [53], uniGradICON [47], and MultiGradICON [13], we use their official implementations and adopt the optimal hyperparameters as specified in their respective publications. Finally, for the fully supervised CNN, we train a 3D CNN model with the same architecture as our proposed anatomical landmark detection model (detailed in Sec. 3.3) in a supervised manner using labeled datasets described in Sec. 4.1. For this model, we use the MSE loss function and maintain the same training parameters as our original training detailed in Sec. 4.2. It should be noted that we did not test this supervised CNN on the HCP-T2W dataset because, despite incorporating contrast augmentation during training, the number of annotated T2W samples available was very limited.

## 4.4. Results

Table 1 shows the results across three datasets: HCP T1w, OASIS, and SNSX. The evaluation metrics include MRE in millimeters and SDR (%) at thresholds of 3mm, 6mm, and 9mm. Our proposed method, **CAMLD**, consistently achieved the best results on all datasets. On HCP T1w, it obtained the lowest MRE of  $3.27 \pm 2.24$  mm and the highest SDRs of 54.48% at 3 mm, 93.69% at 6 mm, and 98.94% at 9 mm. For the OASIS dataset, **CAMLD** recorded an MRE of  $3.89 \pm 2.69$  mm with SDRs of 39.24%, 87.15%, and 98.22%. On SNSX, the method achieved an MRE of  $5.11 \pm 3.19$  mm and SDRs of 29.63%, 71.01%, and 91.44%. Compared to other methods, **CAMLD** outperformed both traditional techniques like 3D SIFT and NiftyReg and DL-based methods, such as KeyMorph, BrainMorph, uniGradICON, and MultiGradICON ( $p < 0.05$ ). Importantly, **CAMLD** could outperform the supervised 3D CNN with statistical significance ( $p < 0.05$ ).

To check if **CAMLD** can generalize on other MRI contrasts, we evaluated it on the HCP T2w dataset. Table 2 shows the results of different models on the HCP T2w dataset. Although our model has only been trained on T1w scans, we can see that it could outperform the other baseline methods on the T2w scans. Specifically, **CAMLD** achieved an MRE of  $3.99 \pm 2.25$  mm, which is comparable to the best-performing method, ANTs (MI), at  $3.91 \pm 2.19$ mm. Notably, **CAMLD** attained the highest SDR at the 6mm (86.43%) and 9mm (98.99%) thresholds, surpassing all other methods. While its SDR at the 3 mm threshold (27.19%) was slightly lower than that of ANTs (MI) (35.00%) and MultiGradICON (33.33%), **CAMLD** still demonstrated strong performance given it was not trained on T2w images.

Table 1. Comparing landmark detection test performance across three datasets: HCP T1w, OASIS, and SNSX.

| Method                  | Metric            | HCP T1w            |               |               |               | OASIS              |               |               |               | SNSX               |               |               |               |
|-------------------------|-------------------|--------------------|---------------|---------------|---------------|--------------------|---------------|---------------|---------------|--------------------|---------------|---------------|---------------|
|                         |                   | MRE (mm) ↓         | SDR (3mm) ↑   | SDR (6mm) ↑   | SDR (9mm) ↑   | MRE (mm) ↓         | SDR (3mm) ↑   | SDR (6mm) ↑   | SDR (9mm) ↑   | MRE (mm) ↓         | SDR (3mm) ↑   | SDR (6mm) ↑   | SDR (9mm) ↑   |
| 3D SIFT [36]            | -                 | 39.44 ± 31.02      | 5.72%         | 20.62%        | 26.97%        | 39.08 ± 29.70      | 3.70%         | 17.71%        | 24.88%        | 41.67 ± 31.84      | 4.52%         | 17.13%        | 25.43%        |
| NiftyReg [29]           | NMI               | 4.43 ± 2.42        | 25.00%        | 81.25%        | 96.04%        | 8.23 ± 3.29        | 1.85%         | 22.69%        | 65.16%        | 9.61 ± 4.03        | 0.43%         | 12.71%        | 50.11%        |
| ANTs [3]                | CC                | 3.85 ± 2.26        | 36.97%        | 89.16%        | 97.54%        | 4.38 ± 2.64        | 29.39%        | 81.25%        | 97.33%        | 6.36 ± 3.28        | 10.88%        | 49.78%        | 87.39%        |
| ANTs [3]                | MI                | 3.65 ± 2.29        | 45.52%        | 92.29%        | 98.85%        | 4.15 ± 2.65        | 38.88%        | 85.38%        | 97.91%        | 6.06 ± 3.22        | 18.75%        | 54.43%        | 90.73%        |
| KeyMorph (64 KPs) [52]  | Dice              | 8.05 ± 4.51        | 10.93%        | 38.43%        | 62.60%        | 8.20 ± 4.64        | 10.30%        | 36.57%        | 63.88%        | 9.73 ± 5.35        | 6.03%         | 31.35%        | 57.86%        |
| KeyMorph (128 KPs) [52] | Dice              | 5.77 ± 2.91        | 13.95%        | 58.43%        | 89.47%        | 6.41 ± 3.41        | 13.31%        | 51.62%        | 81.71%        | 8.99 ± 4.16        | 3.66%         | 25.43%        | 54.95%        |
| KeyMorph (256 KPs) [52] | Dice              | 5.37 ± 3.12        | 20.83%        | 66.04%        | 88.96%        | 6.44 ± 3.81        | 12.61%        | 55.20%        | 81.94%        | 8.80 ± 5.22        | 7.65%         | 35.56%        | 59.48%        |
| KeyMorph (512 KPs) [52] | Dice              | 4.67 ± 2.47        | 23.30%        | 78.12%        | 95.80%        | 7.15 ± 3.63        | 6.82%         | 40.97%        | 75.81%        | 5.77 ± 3.27        | 18.10%        | 60.66%        | 87.82%        |
| BrainMorph [53]         | MSE+Dice          | 4.11 ± 2.30        | 31.35%        | 86.15%        | 97.81%        | 5.28 ± 3.07        | 17.36%        | 74.31%        | 90.39%        | 13.66 ± 18.21      | 14.66%        | 41.38%        | 61.85%        |
| uniGradICON [47]        | LNCC              | 4.12 ± 2.53        | 34.38%        | 84.06%        | 97.29%        | 4.63 ± 3.00        | 30.09%        | 76.97%        | 93.29%        | 5.27 ± 3.53        | 29.53%        | 70.63%        | 88.90%        |
| MultiGradICON [13]      | LNCC <sup>2</sup> | 4.10 ± 2.56        | 34.90%        | 84.17%        | 96.67%        | 4.62 ± 3.01        | 30.79%        | 77.89%        | 93.52%        | 5.21 ± 3.40        | 28.68%        | 70.84%        | 89.12%        |
| Fully Supervised 3D CNN | -                 | 4.65 ± 2.40        | 24.27%        | 72.81%        | 95.42%        | 4.53 ± 2.81        | 25.00%        | 79.28%        | 94.44%        | 6.64 ± 3.86        | 12.61%        | 52.26%        | 76.19%        |
| <b>CAMLD (ours)</b>     | <b>MSE</b>        | <b>3.27 ± 2.24</b> | <b>54.48%</b> | <b>93.69%</b> | <b>98.94%</b> | <b>3.89 ± 2.69</b> | <b>39.24%</b> | <b>87.15%</b> | <b>98.22%</b> | <b>5.11 ± 3.19</b> | <b>29.63%</b> | <b>71.01%</b> | <b>91.44%</b> |

Table 2. Comparing landmark detection performance on HCP-T2w test dataset.

| Method                  | Metric            | MRE (mm) ↓         | SDR (3mm) ↑   | SDR (6mm) ↑   | SDR (9mm) ↑   |
|-------------------------|-------------------|--------------------|---------------|---------------|---------------|
| 3D SIFT [36]            | -                 | 54.90 ± 24.51      | 0.00%         | 0.73%         | 1.35%         |
| NiftyReg [29]           | NMI               | 4.40 ± 2.41        | 25.50%        | 82.25%        | 96.28%        |
| ANTs [3]                | MI                | <b>3.91 ± 2.19</b> | <b>35.00%</b> | 84.27%        | 98.64%        |
| KeyMorph (64 KPs) [52]  | Dice              | 6.00 ± 2.64        | 11.87%        | 52.08%        | 88.33%        |
| KeyMorph (128 KPs) [52] | Dice              | 8.66 ± 4.29        | 5.93%         | 28.64%        | 58.23%        |
| KeyMorph (256 KPs) [52] | Dice              | 6.41 ± 3.06        | 8.65%         | 51.56%        | 83.54%        |
| KeyMorph (512 KPs) [52] | Dice              | 5.54 ± 3.31        | 22.18%        | 64.06%        | 85.62%        |
| BrainMorph [53]         | MSE+Dice          | 4.24 ± 2.43        | 32.71%        | 82.19%        | 96.77%        |
| uniGradICON [47]        | LNCC              | 13.44 ± 3.88       | 0.42%         | 3.33%         | 12.60%        |
| MultiGradICON [13]      | LNCC <sup>2</sup> | 4.31 ± 2.70        | 33.33%        | 81.83%        | 95.83%        |
| <b>CAMLD (ours)</b>     | <b>MSE</b>        | <b>3.99 ± 2.25</b> | <b>27.19%</b> | <b>86.43%</b> | <b>98.99%</b> |

Table 3. Testing the influence of contrast augmentation with RC and consistency loss ( $\mathcal{L}_{\text{consistency}}$ ) on the proposed framework using landmark MRE (mm) across all datasets.

| Methods                              | HCP-T1w                 | OASIS                   | SNSX                    | HCP-T2w                   |
|--------------------------------------|-------------------------|-------------------------|-------------------------|---------------------------|
| Base Model                           | 53.69 ± 25.63           | 55.02 ± 25.68           | 53.11 ± 29.18           | 59.79 ± 26.39             |
| + $\mathcal{L}_{\text{consistency}}$ | 3.70 ± 2.41<br>(-49.99) | 4.03 ± 2.69<br>(-50.99) | 6.43 ± 3.64<br>(-46.68) | 45.90 ± 17.77<br>(-13.89) |
| +RC                                  | 3.27 ± 2.24<br>(-0.43)  | 3.89 ± 2.69<br>(-0.14)  | 5.11 ± 3.59<br>(-1.32)  | 3.99 ± 2.25<br>(-41.91)   |

#### 4.5. Ablation Studies

We conducted ablation studies to assess the impact of the consistency loss ( $\mathcal{L}_{\text{consistency}}$ ) and contrast augmentation with RC on our model’s performance, as shown in Table 3. Adding  $\mathcal{L}_{\text{consistency}}$  to the base model drastically reduced the Mean Radial Error across all datasets. For example, on HCP T1w, the MRE decreased from 53.69 ± 25.63 mm to 3.70 ± 2.41 mm. Incorporating RC further improved the MRE, notably reducing it to 3.99 ± 2.25 mm on HCP-T2w. These results demonstrate that both  $\mathcal{L}_{\text{consistency}}$  and RC are essential for enhancing the model’s accuracy and generalization across different datasets.

Different head orientations in the MRI scans can occur

due to patient positioning, between-scan movement, and scanner setup, but they could affect the quality of landmark detection [7, 43]. Therefore, to assess the robustness of CAMLD against this factor, we have evaluated its performance under conditions of augmented rotation misalignments to each scan. Figure 3 illustrates the MRE as a function of the augmented rotation. Our analysis reveals that while methods, such as ANTs perform adequately with very minimal augmented misalignment, their performance declines quickly as the additional rotation increases. In contrast, CAMLD demonstrates robust and consistent performance across a wide range of transformations even under large misalignments, without notable performance drops.

#### 5. Discussion

Different from the previous landmark-based registration methods [5, 6, 16, 52, 53], which produce spontaneous anatomical landmarks to explain registration results and regularize image alignment, CAMLD specifically focuses on accurate anatomical landmarks that are consistent with a pre-defined protocol. We achieve this by incorporating subject-template and cross-subject consistency loss functions, with the injection of expert knowledge using a population-averaged MRI atlas. This greatly reduces the

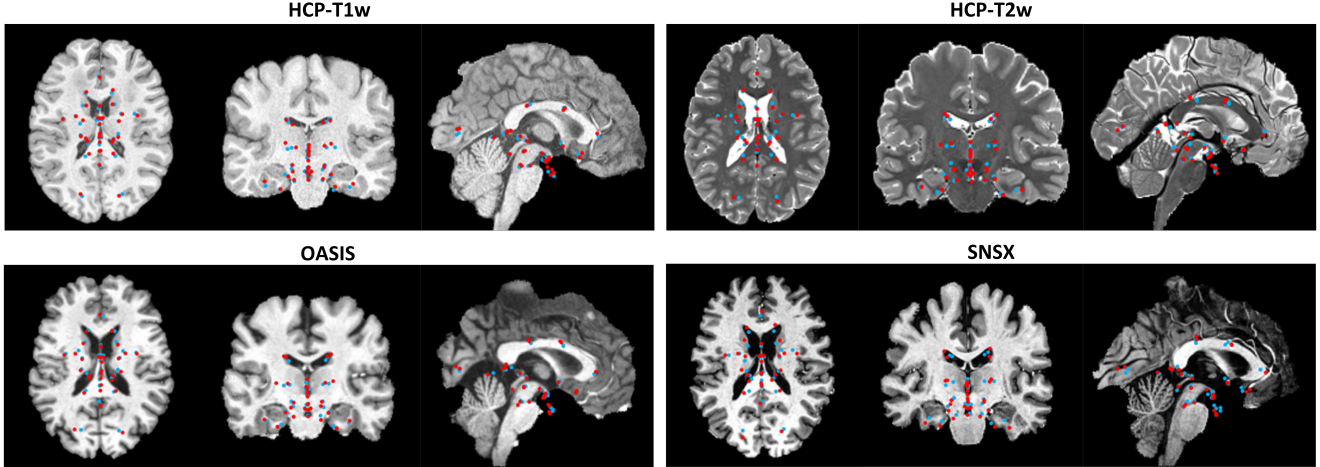


Figure 2. Qualitative comparison of anatomical landmark detection results using the proposed technique, illustrated on coronal, axial, and sagittal mid-slices (red=ground truths, blue=automatic results) for samples across all datasets. Note that the landmarks shown are projections of 3D points in each canonical view.

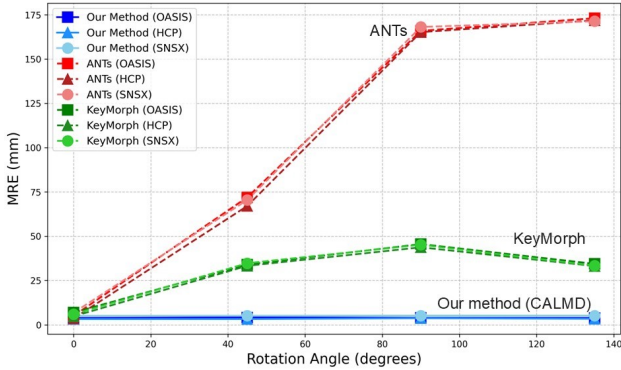


Figure 3. Comparison of different methods' MRE (mm) performance across varying levels of added rotation misalignments.

demand for large amounts of annotated data in model training. Note that as a reference atlas is involved during the training, which allows landmark discovery in individuals to adapt to the references, our approach deviates from the conventional one-shot learning strategy. As our aim is to detect clinically significant anatomical landmarks, **CAML**D prioritizes accurate landmark correspondence over full volumetric registration. Thus, the resulting deformation fields produced by the algorithm may not achieve registration accuracy globally, in comparison to registration-specific DL algorithms. In this regard, we employed an adaptive mixed loss function, gradually shifting the focus from registration to consistency regularization during training. By first learning the general spatial relationship of the anatomical context and then refining predictions to align with anatomically significant landmarks, our framework balances the need for both alignment and anatomical consistency.

Our method's robustness to multi-center MRI data with different field strengths and unseen contrasts fortifies its potential in clinical applications. The use of random convolution offers a simpler and more robust way to allow contrast-agnostic landmark detection than more traditional contrast augmentation methods, which fail to address the domain-specific concerns in radiological AI. Compared with stochastic intensity transformation [30], RC simulates richer and more nuanced contrasts due to the use of consecutive convolutions. To the best of our knowledge, we are the first to adopt 3D RC in medical image analysis and specifically, contrast-agnostic anatomical landmark detection.

In our framework,  $M$  training samples can be used to enforce the cross-subject and subject-template consistency. While a larger  $M$  is desirable, a trade-off with the hardware resource needs to be considered. To ensure brain landmark localization precision, we used high-resolution MRI inputs, limiting the choice of  $M$  to 2. However, with smaller data, a larger  $M$  can potentially be accommodated, and we will study the impacts in the future.

## 6. Conclusion

We proposed **CAML**D, a novel and annotation-efficient framework for contrast-agnostic medical landmark detection, with the requirement of only a single reference annotation. Our method leverages consistency-based regularization and RC to accurately detect anatomical landmarks and encourage the generalization to unseen contrasts. Thorough validation has confirmed that our method achieves SOTA accuracy compared with existing methods. Notably, **CAML**D shows strong robustness against anatomical misalignment from the reference scan.



## References

- [1] Mohamad Abbass, Greydon Gilmore, Alaa Taha, Ryan Chevalier, Magdalena Jach, Terry M Peters, Ali R Khan, and Jonathan C Lau. Application of the anatomical fiducials framework to a clinical dataset of patients with parkinson’s disease. *Brain Structure and Function*, pages 1–13, 2022. 1
- [2] Anneke Alkemade, Martijn J Mulder, Josephine M Groot, Bethany R Isaacs, Nikita van Berendonk, Nicky Lute, Scott JS Isherwood, Pierre-Louis Bazin, and Birte U Forstmann. The Amsterdam Ultra-high field adult lifespan database (AHEAD): A freely available multimodal 7 Tesla submillimeter magnetic resonance imaging database. *NeuroImage*, 221:117200, 2020. 5
- [3] Brian B Avants, Nick Tustison, Gang Song, et al. Advanced normalization tools (ANTs). *Insight j*, 2(365):1–35, 2009. 2, 6, 7
- [4] Yoshua Bengio, Jérôme Louradour, Ronan Collobert, and Jason Weston. Curriculum learning. In *International Conference on Machine Learning*, pages 41–48, 2009. 3, 5
- [5] Riddhish Bhalodia, Ladislav Kavan, and Ross T Whitaker. Self-supervised discovery of anatomical shape landmarks. In *Medical Image Computing and Computer Assisted*, pages 627–638. Springer, 2020. 2, 3, 7
- [6] Riddhish Bhalodia, Shireen Elhabian, Ladislav Kavan, and Ross Whitaker. Leveraging unsupervised image registration for discovery of landmark shape descriptor. *Medical Image Analysis*, 73:102157, 2021. 2, 3, 7
- [7] Benjamin Billot, Neel Dey, Daniel Moyer, Malte Hoffmann, Esra Abaci Turk, Borjan Gagoski, P Ellen Grant, and Polina Golland. SE (3)-equivariant and noise-invariant 3D rigid motion tracking in brain MRI. *IEEE Transactions on Medical Imaging*, 2024. 7
- [8] Fred L. Bookstein. Principal warps: Thin-plate splines and the decomposition of deformations. *IEEE Transactions on Pattern Analysis and Machine Intelligence*, 11(6):567–585, 1989. 1
- [9] Bjorn Browatzki and Christian Wallraven. 3fabrec: Fast few-shot face alignment by reconstruction. In *Proceedings of the IEEE/CVF Conference on Computer Vision and Pattern Recognition*, pages 6110–6120, 2020. 2, 3
- [10] Chun-Hung Chao and Marc Niethammer. Self-supervised landmark learning with deformation reconstruction and cross-subject consistency objectives. In *International Workshop on Predictive Intelligence In Medicine*, pages 70–82. Springer, 2023. 2, 3
- [11] Junyu Chen, Yihao Liu, Shuwen Wei, Zhangxing Bian, Shalini Subramanian, Aaron Carass, Jerry L Prince, and Yong Du. A survey on deep learning in medical image registration: New technologies, uncertainty, evaluation metrics, and beyond. *Medical Image Analysis*, page 103385, 2024. 3
- [12] Xiaoyang Chen, Chunfeng Lian, Hannah H Deng, Tianshu Kuang, Hung-Ying Lin, Deqiang Xiao, Jaime Gateno, Ding-gang Shen, James J Xia, and Pew-Thian Yap. Fast and accurate craniomaxillofacial landmark detection via 3D faster R-CNN. *IEEE Transactions on Medical Imaging*, 40(12):3867–3878, 2021. 1, 2, 3
- [13] Başar Demir, Lin Tian, Hastings Greer, Roland Kwitt, François-Xavier Vialard, Raúl San José Estépar, Sylvain Bouix, Richard Rushmore, Ebrahim Ebrahim, and Marc Niethammer. MultiGradICON: A Foundation Model for Multimodal Medical Image Registration. In *International Workshop on Biomedical Image Registration*, pages 3–18. Springer, 2024. 6, 7
- [14] Gianluca Donato and Serge Belongie. Approximate thin plate spline mappings. In *Computer Vision—ECCV 2002: 7th European Conference on Computer Vision Copenhagen, Denmark, May 28–31, 2002 Proceedings, Part III 7*, pages 21–31. Springer, 2002. 1
- [15] Simon F Eskildsen, Pierrick Coupé, Vladimir Fonov, José V Manjón, Kelvin K Leung, Nicolas Guizard, Shafik N Wassef, Lasse Riis Østergaard, D Louis Collins, Alzheimer’s Disease Neuroimaging Initiative, et al. Beast: brain extraction based on nonlocal segmentation technique. *NeuroImage*, 59(3):2362–2373, 2012. 5
- [16] M Yu Evan, Alan Q Wang, Adrian V Dalca, and Mert R Sabuncu. KeyMorph: Robust multi-modal affine registration via unsupervised keypoint detection. In *Medical Imaging with Deep Learning*, 2022. 2, 7
- [17] Vladimir S Fonov, Alan C Evans, Robert C McKinsty, C Robert Almlı, and DL Collins. Unbiased nonlinear average age-appropriate brain templates from birth to adulthood. *NeuroImage*, 47:S102, 2009. 5
- [18] Günther Grabner, Andrew L Janke, Marc M Budge, David Smith, Jens Pruessner, and D Louis Collins. Symmetric atlasing and model based segmentation: an application to the hippocampus in older adults. In *International Conference on Medical Image Computing and Computer Assisted Intervention*, pages 58–66. Springer, 2006. 5
- [19] Malte Hoffmann, Benjamin Billot, Douglas N Greve, Juan Eugenio Iglesias, Bruce Fischl, and Adrian V Dalca. Synthmorph: learning contrast-invariant registration without acquired images. *IEEE Transactions on Medical Imaging*, 41(3):543–558, 2021. 2
- [20] Sina Honari, Pavlo Molchanov, Stephen Tyree, Pascal Vincent, Christopher Pal, and Jan Kautz. Improving landmark localization with semi-supervised learning. In *Proceedings of the IEEE Conference on Computer Vision and Pattern Recognition*, pages 1546–1555, 2018. 3
- [21] Florian Kordon, Peter Fischer, Maxim Privalov, Benedict Swartman, Marc Schnetzke, Jochen Franke, Ruxandra Lasowski, Andreas Maier, and Holger Kunze. Multi-task localization and segmentation for X-Ray guided planning in knee surgery. In *International Conference on Medical Image Computing and Computer Assisted Intervention*, pages 622–630. Springer, 2019. 1
- [22] Yankun Lang, Li Wang, Pew-Thian Yap, Chunfeng Lian, Hannah Deng, Kim-Han Thung, Deqiang Xiao, Peng Yuan, Steve GF Shen, Jaime Gateno, et al. Automatic detection of craniomaxillofacial anatomical landmarks on CBCT images using 3D mask R-CNN. In *International Workshop on Graph Learning in Medical Imaging*, pages 130–137. Springer, 2019. 2, 3
- [23] Yankun Lang, Chunfeng Lian, Deqiang Xiao, Hannah Deng, Peng Yuan, Jaime Gateno, Steve GF Shen, David M Alfı,

- Pew-Thian Yap, James J Xia, et al. Automatic localization of landmarks in craniomaxillofacial CBCT images using a local attention-based graph convolution network. In *International Conference on Medical Image Computing and Computer Assisted Intervention*, pages 817–826. Springer, 2020. 3
- [24] Jupeng Li, Yinghui Wang, Junbo Mao, Gang Li, and Ruohan Ma. End-to-end coordinate regression model with attention-guided mechanism for landmark localization in 3D medical images. In *International Workshop on Machine Learning in Medical Imaging*, pages 624–633. Springer, 2020. 3
- [25] Chunfeng Lian, Fan Wang, Hannah H Deng, Li Wang, Deqiang Xiao, Tianshu Kuang, Hung-Ying Lin, Jaime Gateno, Steve GF Shen, Pew-Thian Yap, et al. Multi-task dynamic transformer network for concurrent bone segmentation and large-scale landmark localization with dental CBCT. In *International Conference on Medical Image Computing and Computer Assisted Intervention*. Springer, 2020. 2, 3
- [26] Tianyu Ma, Ajay Gupta, and Mert R Sabuncu. Volumetric landmark detection with a multi-scale shift equivariant neural network. In *2020 IEEE 17th International Symposium on Biomedical Imaging (ISBI)*, pages 981–985. IEEE, 2020. 5
- [27] Daniel S Marcus, Tracy H Wang, Jamie Parker, John G Csernansky, John C Morris, and Randy L Buckner. Open access series of imaging studies (OASIS): cross-sectional MRI data in young, middle aged, nondemented, and demented older adults. *Journal of Cognitive Neuroscience*, 19(9):1498–1507, 2007. 5
- [28] James McCouat and Irina Voiculescu. Contour-hugging heatmaps for landmark detection. In *Proceedings of the IEEE/CVF Conference on Computer Vision and Pattern Recognition*, pages 20597–20605, 2022. 1, 3
- [29] Marc Modat, Gerard R Ridgway, Zeike A Taylor, Manja Lehmann, Josephine Barnes, David J Hawkes, Nick C Fox, and Sébastien Ourselin. Fast free-form deformation using graphics processing units. *Computer Methods and Programs in Biomedicine*, 98(3):278–284, 2010. 2, 6, 7
- [30] Tony CW Mok, Zi Li, Yunhao Bai, Jianpeng Zhang, Wei Liu, Yan-Jie Zhou, Ke Yan, Dakai Jin, Yu Shi, Xiaoli Yin, et al. Modality-Agnostic Structural Image Representation Learning for Deformable Multi-Modality Medical Image Registration. In *Proceedings of the IEEE/CVF Conference on Computer Vision and Pattern Recognition*, pages 11215–11225, 2024. 8
- [31] Abbas Omid, Aida Mohammadshahi, Neha Gianchandani, Regan King, Lara Leijser, and Roberto Souza. Unsupervised domain adaptation of MRI skull-stripping trained on adult data to newborns. In *Proceedings of the IEEE/CVF Winter Conference on Applications of Computer Vision*, pages 7718–7727, 2024. 4
- [32] Abbas Omid, Amirmohammad Shamaei, Anouk Verschu, Regan King, Lara Leijser, and Roberto Souza. Unsupervised domain adaptation of brain MRI skull stripping trained on adult data to newborns: Combining synthetic data with domain invariant features. In *Medical Imaging with Deep Learning*, 2024. 4
- [33] Cheng Ouyang, Chen Chen, Surui Li, Zeju Li, Chen Qin, Wenjia Bai, and Daniel Rueckert. Causality-inspired single-source domain generalization for medical image segmentation. *IEEE Transactions on Medical Imaging*, 42(4):1095–1106, 2022. 2, 5
- [34] Quan Quan, Qingsong Yao, Jun Li, and S Kevin Zhou. Which images to label for few-shot medical landmark detection? In *Proceedings of the IEEE/CVF Conference on Computer Vision and Pattern Recognition*, pages 20606–20616, 2022. 1
- [35] Quan Quan, Qingsong Yao, Heqin Zhu, Qiyuan Wang, and S Kevin Zhou. Which images to label for few-shot medical image analysis? *Medical Image Analysis*, 96:103200, 2024. 1
- [36] Blaine Rister, Mark A Horowitz, and Daniel L Rubin. Volumetric image registration from invariant keypoints. *IEEE Transactions on Image Processing*, 26(10):4900–4910, 2017. 6, 7
- [37] Torsten Rohlfing. Image similarity and tissue overlaps as surrogates for image registration accuracy: widely used but unreliable. *IEEE Transactions on Medical Imaging*, 31(2): 153–163, 2011. 1
- [38] Karl Rohr, H Siegfried Stiehl, Rainer Sprengel, Thorsten M Buzug, Jürgen Weese, and MH Kuhn. Landmark-based elastic registration using approximating thin-plate splines. *IEEE Transactions on Medical Imaging*, 20(6):526–534, 2001. 1
- [39] Soorena Salari, Amirhossein Rasouljan, Michele Battie, Maryse Fortin, Hassan Rivaz, and Yiming Xiao. Uncertainty-aware transformer model for anatomical landmark detection in paraspinal muscle MRIs. In *Medical Imaging 2023: Image Processing*, pages 246–252. SPIE, 2023. 1
- [40] Roni Setton, Laetitia Mwilambwe-Tshilobo, Manesh Girm, Amber W Lockrow, Giulia Baracchini, Colleen Hughes, Alexander J Lowe, Benjamin N Cassidy, Jian Li, Wen-Ming Luh, et al. Age differences in the functional architecture of the human brain. *Cerebral Cortex*, 33(1):114–134, 2023. 5
- [41] Mostafa Sharifzadeh, Sobhan Goudarzi, An Tang, Habib Benali, and Hassan Rivaz. Mitigating aberration-induced noise: A deep learning-based aberration-to-aberration approach. *IEEE Transactions on Medical Imaging*, 2024. 4
- [42] Vasiliki Sideri-Lampretsa, Veronika A Zimmer, Huaqi Qiu, Georgios Kaissis, and Daniel Rueckert. MAD: Modality agnostic distance measure for image registration. In *International Conference on Medical Image Computing and Computer-Assisted Intervention*, pages 147–156. Springer, 2023. 2, 5
- [43] Nalini M Singh, Neel Dey, Malte Hoffmann, Bruce Fischl, Elfar Adalsteinsson, Robert Frost, Adrian V Dalca, and Polina Golland. Data consistent deep rigid MRI motion correction. In *Medical Imaging with Deep Learning*, pages 368–381. PMLR, 2024. 7
- [44] Michal Sofka, Fausto Milletari, Jimmy Jia, and Alex Rothberg. Fully convolutional regression network for accurate detection of measurement points. In *Deep Learning in Medical Image Analysis and Multimodal Learning for Clinical Decision Support*, pages 258–266. Springer, 2017. 5
- [45] R Nathan Spreng, Roni Setton, Udi Alter, Benjamin N Cassidy, Bri Darboh, Elizabeth DuPre, Karin Kantarovich, Amber W Lockrow, Laetitia Mwilambwe-Tshilobo, Wen-Ming

- Luh, et al. Neurocognitive aging data release with behavioral, structural and multi-echo functional MRI measures. *Scientific Data*, 9(1):119, 2022. 5
- [46] Alaa Taha, Greydon Gilmore, Mohamad Abbass, Jason Kai, Tristan Kuehn, John Demarco, Geetika Gupta, Chris Zajner, Daniel Cao, Ryan Chevalier, et al. Magnetic resonance imaging datasets with anatomical fiducials for quality control and registration. *Scientific Data*, 10(1):449, 2023. 1, 5
- [47] Lin Tian, Hastings Greer, Roland Kwitt, François-Xavier Vialard, Raúl San José Estépar, Sylvain Bouix, Richard Rushmore, and Marc Niethammer. uniGradICON: A Foundation Model for Medical Image Registration. In *International Conference on Medical Image Computing and Computer-Assisted Intervention*, pages 749–760. Springer, 2024. 6, 7
- [48] Jonathan J Tompson, Arjun Jain, Yann LeCun, and Christoph Bregler. Joint training of a convolutional network and a graphical model for human pose estimation. *Advances in Neural Information Processing Systems*, 27, 2014. 1
- [49] Neslisah Torosdagli, Denise K Liberton, Payal Verma, Murat Sincan, Janice S Lee, and Ulas Bagci. Deep geodesic learning for segmentation and anatomical landmarking. *IEEE Transactions on Medical Imaging*, 38(4):919–931, 2018. 3
- [50] Martin Urschler, Christopher Zach, Hendrik Ditt, and Horst Bischof. Automatic point landmark matching for regularizing nonlinear intensity registration: Application to thoracic CT images. In *International Conference on Medical Image Computing and Computer-Assisted Intervention*, pages 710–717. Springer, 2006. 1
- [51] David C Van Essen, Stephen M Smith, Deanna M Barch, Timothy EJ Behrens, Essa Yacoub, Kamil Ugurbil, Wu-Minn HCP Consortium, et al. The WU-Minn human connectome project: an overview. *Neuroimage*, 80:62–79, 2013. 5
- [52] Alan Q Wang, M Yu Evan, Adrian V Dalca, and Mert R Sabuncu. A robust and interpretable deep learning framework for multi-modal registration via keypoints. *Medical Image Analysis*, 90:102962, 2023. 2, 3, 6, 7
- [53] Alan Q Wang, Rachit Saluja, Heejong Kim, Xinzi He, Adrian Dalca, and Mert R Sabuncu. BrainMorph: A Foundational Keypoint Model for Robust and Flexible Brain MRI Registration. *arXiv preprint arXiv:2405.14019*, 2024. 2, 3, 6, 7
- [54] Xin Wang, Yudong Chen, and Wenwu Zhu. A survey on curriculum learning. *IEEE Transactions on Pattern Analysis and Machine Intelligence*, 44(9):4555–4576, 2021. 3, 4, 5
- [55] Yinsong Wang, Siyi Du, Shaoming Zheng, Xinzhe Luo, and Chen Qin. CAR: Contrast-agnostic deformable medical image registration with contrast-invariant latent regularization. In *International Workshop on Biomedical Image Registration*, pages 308–318. Springer, 2024. 2, 5
- [56] Yiming Xiao, Jonathan C Lau, Dimuthu Hemachandra, Greydon Gilmore, Ali R Khan, and Terry M Peters. Image guidance in deep brain stimulation surgery to treat Parkinson’s disease: A comprehensive review. *IEEE Transactions on Biomedical Engineering*, 68(3):1024–1033, 2020. 1
- [57] Yiming Xiao, Greydon Gilmore, Jason Kai, Jonathan C Lau, Terry Peters, and Ali R Khan. A population-averaged structural connectomic brain atlas dataset from 422 HCP-aging subjects. *Data in Brief*, 50:109513, 2023. 2
- [58] Zhenlin Xu, Deyi Liu, Junlin Yang, Colin Raffel, and Marc Niethammer. Robust and generalizable visual representation learning via random convolutions. In *International Conference on Learning Representations*, 2021. 5
- [59] Jingru Yi, Pengxiang Wu, Qiaoying Huang, Hui Qu, and Dimitris N Metaxas. Vertebra-focused landmark detection for scoliosis assessment. In *2020 IEEE 17th International Symposium on Biomedical Imaging (ISBI)*, pages 736–740. IEEE, 2020. 1
- [60] Tianhe Yu, Saurabh Kumar, Abhishek Gupta, Sergey Levine, Karol Hausman, and Chelsea Finn. Gradient surgery for multi-task learning. *Advances in Neural Information Processing Systems*, 33:5824–5836, 2020. 4
- [61] Hye Sun Yun, Tae Jun Jang, Sung Min Lee, Sang-Hwy Lee, and Jin Keun Seo. Learning-based local-to-global landmark annotation for automatic 3D cephalometry. *Physics in Medicine & Biology*, 65(8):085018, 2020. 3
- [62] Jun Zhang, Mingxia Liu, Le An, Yaozong Gao, and Dinggang Shen. Alzheimer’s disease diagnosis using landmark-based features from longitudinal structural MR images. *IEEE Journal of Biomedical and Health Informatics*, 21(6):1607–1616, 2017. 1
- [63] Jun Zhang, Mingxia Liu, and Dinggang Shen. Detecting anatomical landmarks from limited medical imaging data using two-stage task-oriented deep neural networks. *IEEE Transactions on Image Processing*, 26(10):4753–4764, 2017. 1, 3
- [64] Jun Zhang, Mingxia Liu, Li Wang, Si Chen, Peng Yuan, Jianfu Li, Steve Guo-Fang Shen, Zhen Tang, Ken-Chung Chen, James J Xia, et al. Context-guided fully convolutional networks for joint craniomaxillofacial bone segmentation and landmark digitization. *Medical image analysis*, 60:101621, 2020. 3
- [65] Jian Zhao and Hui Zhang. Thin-plate spline motion model for image animation. In *Proceedings of the IEEE/CVF Conference on Computer Vision and Pattern Recognition*, pages 3657–3666, 2022. 1
- [66] Zhushi Zhong, Jie Li, Zhenxi Zhang, Zhicheng Jiao, and Xinbo Gao. An attention-guided deep regression model for landmark detection in cephalograms. In *International Conference on Medical Image Computing and Computer Assisted Intervention*, pages 540–548. Springer, 2019. 1
- [67] Heqin Zhu, Quan Quan, Qingsong Yao, Zaiyi Liu, and S Kevin Zhou. UOD: Universal one-shot detection of anatomical landmarks. In *International Conference on Medical Image Computing and Computer-Assisted Intervention*, pages 24–34. Springer, 2023. 1

# CAMLD: Contrast-Agnostic Medical Landmark Detection with Consistency-Based Regularization

## Supplementary Material

### 1. Research Ethics Approval

This study has received approval from the Research Ethics Board (REB) of the anonymous institute.

### 2. Analytical and Differentiable Coordinate Transformations

**Notation:** Lowercase bold letters denote column vectors, while uppercase bold letters are used for matrices. Coordinates in  $D$  dimensions are represented as column vectors, i.e.,  $\mathbf{x} \in \mathbb{R}^D$ . The symbol  $\tilde{\mathbf{x}}$  denotes  $\mathbf{x}$  in homogeneous coordinates, expressed as  $\tilde{\mathbf{x}} = [\mathbf{x}, 1]^T$ . Superscripts like  $\mathbf{x}^{(j)}$  are used to indicate distinct instances of  $\mathbf{x}$  (such as in a dataset), while subscripts,  $\mathbf{x}_j$ , represent the  $j$ -th component of  $\mathbf{x}$ .

We introduce families of parametric transformations that can be derived explicitly in closed-form based on corresponding landmark pairs. Let us consider  $N$  matching landmark pairs  $\{(\mathbf{x}^{(j)}, \mathbf{y}^{(j)})\}_{j=1}^N$ , where  $\mathbf{x}^{(j)}, \mathbf{y}^{(j)} \in \mathbb{R}^D$  and  $N > D$ . For simplicity, we define  $\mathbf{X} := \langle \mathbf{x}^{(1)} \dots \mathbf{x}^{(N)} \rangle \in \mathbb{R}^{D \times N}$ , and similarly for  $\tilde{\mathbf{X}}$  and  $\mathbf{Y}$ . We define a transformation function  $T_\beta : \mathbb{R}^D \rightarrow \mathbb{R}^D$ , where  $\beta \in \mathcal{B}$  are the transformation parameters.

#### 2.1. Thin-Plate Spline Deformation Model

The thin-plate spline (TPS) transformation is used for coordinate mapping, delivering a non-rigid, parameterized deformation model with a closed-form solution for interpolating corresponding landmarks [8, 14, 38, 65]. This approach offers greater adaptability than affine mappings while inherently encompassing affine transformations as a specific case.

The TPS deformation model  $T_\beta : \mathbb{R}^D \rightarrow \mathbb{R}^D$  is expressed as:

$$T_\beta(\mathbf{x}) = \mathbf{W}^T \tilde{\mathbf{x}} + \sum_{j=1}^N \mathbf{v}_j \Phi(\|\mathbf{x}^{(j)} - \mathbf{x}\|^2), \quad (\text{S1})$$

where  $\mathbf{W} \in \mathbb{R}^{D \times (D+1)}$  and  $\mathbf{v}_j \in \mathbb{R}^D$  represent the transformation parameters ( $\beta$ ), and  $\Phi(r) = r^2 \ln(r)$ . Additionally,  $\mathbf{V} = \{\mathbf{v}_j\}_{j=1}^N$ , making the full parameter set  $\beta = \{\mathbf{W}, \mathbf{V}\}$ .

The transformation  $T$  minimizes the bending energy:

$$I_T = \int_{\mathbb{R}^D} \|\nabla^2 T(\mathbf{x})\|_F^2 d\mathbf{x}, \quad (\text{S2})$$

which ensures that  $T$  is smooth with square-integrable second derivatives. We impose the interpolation conditions  $T(\mathbf{x}^{(j)}) = \mathbf{y}^{(j)}$  for  $j = 1, \dots, N$ , and the following constraints to ensure a well-posed solution:

$$\sum_{j=1}^N \mathbf{v}_j = \mathbf{0} \quad \text{and} \quad \sum_{j=1}^N \mathbf{v}_j (\mathbf{x}^{(j)})^T = \mathbf{0}. \quad (\text{S3})$$

Based on the mentioned conditions, the linear system below can be considered for  $\beta$ :

$$\begin{bmatrix} \mathbf{M} & \mathbf{R} \\ \mathbf{R}^T & \mathbf{Z} \end{bmatrix} \begin{bmatrix} \mathbf{V} \\ \mathbf{W} \end{bmatrix} = \begin{bmatrix} \mathbf{Y} \\ \mathbf{Z} \end{bmatrix}, \quad (\text{S4})$$

where  $\mathbf{M} \in \mathbb{R}^{N \times N}$  with entries  $M_{ij} = \Phi(\|\mathbf{x}^{(i)} - \mathbf{x}^{(j)}\|^2)$ ,  $\mathbf{R} \in \mathbb{R}^{N \times (D+1)}$  where each Row  $j$  is  $\tilde{\mathbf{x}}^{(j)T}$ ,  $\mathbf{V} \in \mathbb{R}^{N \times D}$  with the  $j$ th row being  $\mathbf{v}_j^T$ ,  $\mathbf{Y} \in \mathbb{R}^{N \times D}$  with row entries of  $\mathbf{y}^{(j)T}$ , and  $\mathbf{Z}$  is a zero matrix with the proper size.

Accordingly, the solution  $\beta^*$  is obtained by:

$$\beta^* = \begin{bmatrix} \mathbf{V}^* \\ \mathbf{W}^* \end{bmatrix} = \begin{bmatrix} \mathbf{M} & \mathbf{R} \\ \mathbf{R}^T & \mathbf{Z} \end{bmatrix}^{-1} \begin{bmatrix} \mathbf{Y} \\ \mathbf{Z} \end{bmatrix}. \quad (\text{S5})$$

Using the equations above,  $\beta^*$  can be formulated as a differentiable function, ensuring integration with gradient-based optimization frameworks.

Finally, the general TPS equation can be improved (e.g., to handle noise) by incorporating a regularization term:

$$\beta^* = \arg \min_{\beta} \sum_{j=1}^N \|T_\beta(\mathbf{x}^{(j)}) - \mathbf{y}^{(j)}\|^2 + \lambda I_T, \quad (\text{S6})$$

where  $\lambda$  is a positive hyperparameter that determines the regularization level. As  $\lambda \rightarrow \infty$ , the optimal transformation  $T$  tends to an affine form. This can be achieved by modifying the matrix  $\mathbf{M}$  to  $\mathbf{M} + \lambda \mathbf{I}$  in the linear system (Eq. S4). The parameter  $\lambda$  could influence the solution  $\beta^*$ , leading it either toward an affine transformation as  $\lambda \rightarrow \infty$  or toward a fully nonlinear deformation as  $\lambda \rightarrow 0$ .

### 3. Random Convolution-Based Contrast Augmentation

Figure S1 illustrates the model architecture used for random convolution (RC)-based contrast augmentation. The model consists of five non-linear blocks, each comprising an RC layer followed by a LeakyReLU activation. This cascaded design efficiently captures complex and non-linear intensity

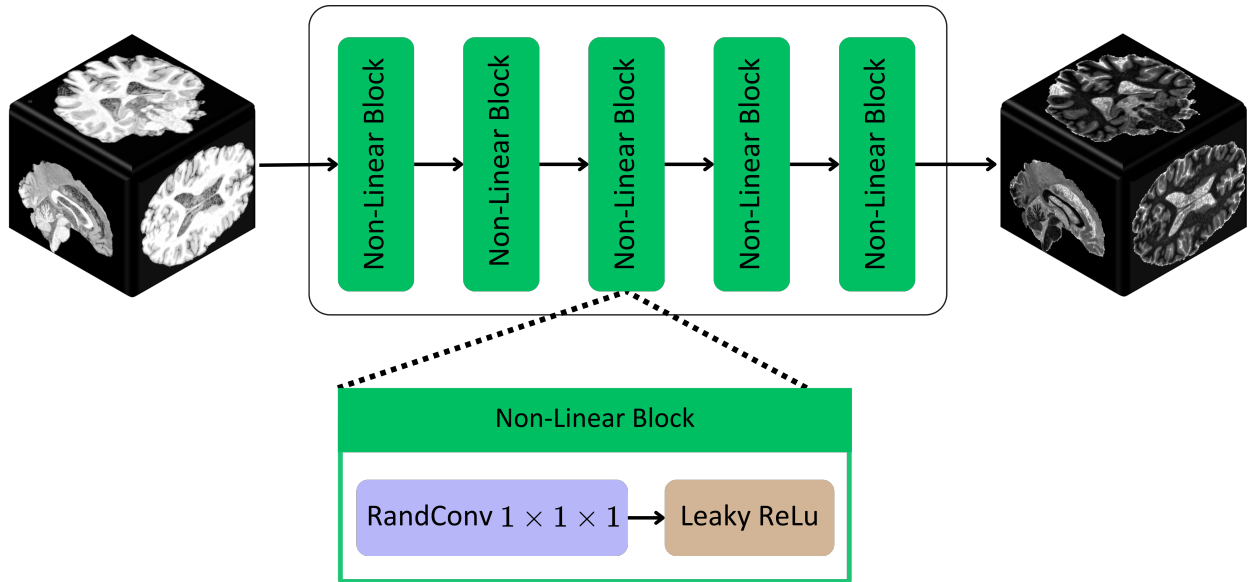


Figure S1. The overall architecture of the proposed 3D contrast augmentation method using random convolution.

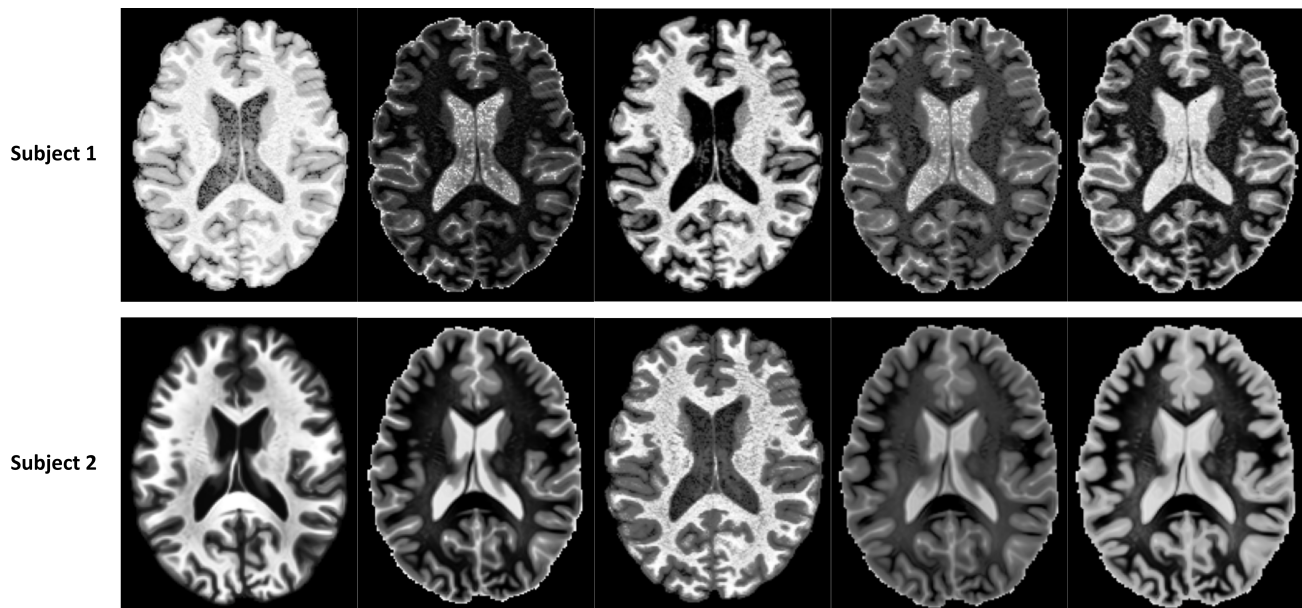


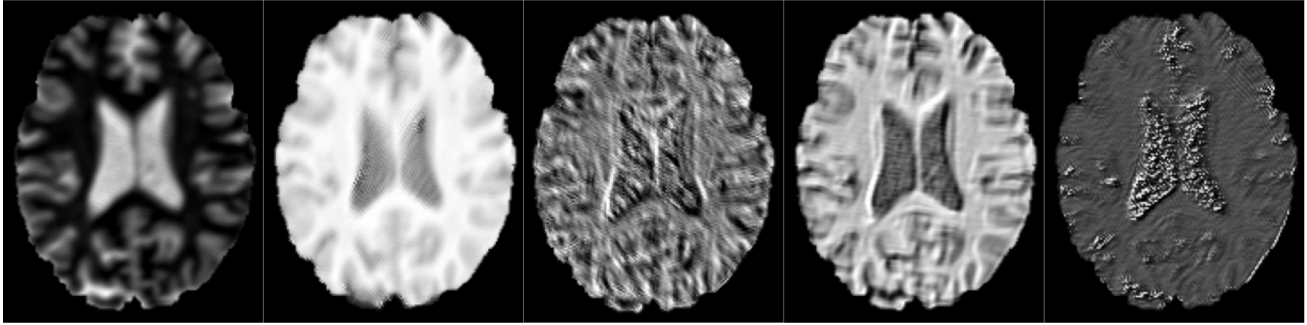
Figure S2. Axial mid-slices of augmented samples generated using the RC-based contrast augmentation method with  $1 \times 1 \times 1$  convolution kernels.

relationships across various MRI contrasts, generating diverse artificial contrast variations from a single scan. Additionally, Figure S2 presents axial mid-slices of augmented samples generated using the RC-based contrast augmentation scheme. These samples demonstrate the effectiveness of RC in simulating a wide range of artificial contrasts from a single input scan.

To investigate the kernel size's impact on the RC output for contrast augmentation, we have implemented the kernel

size of  $3 \times 3 \times 3$  and  $5 \times 5 \times 5$  in all non-linear blocks of our model. Figure S3 showcases axial mid-slices of augmented samples produced using the RC-based contrast augmentation method, incorporating  $3 \times 3 \times 3$  and  $5 \times 5 \times 5$  convolutions. Evidently, in these samples, the augmented outputs exhibit a noticeable blurring effect, which can adversely affect the performance of the DL models. In particular, this blurring compromises precise voxel-to-voxel correspondences for our task, thereby degrading the accuracy

Random Convolution  $3 \times 3 \times 3$



Random Convolution  $5 \times 5 \times 5$

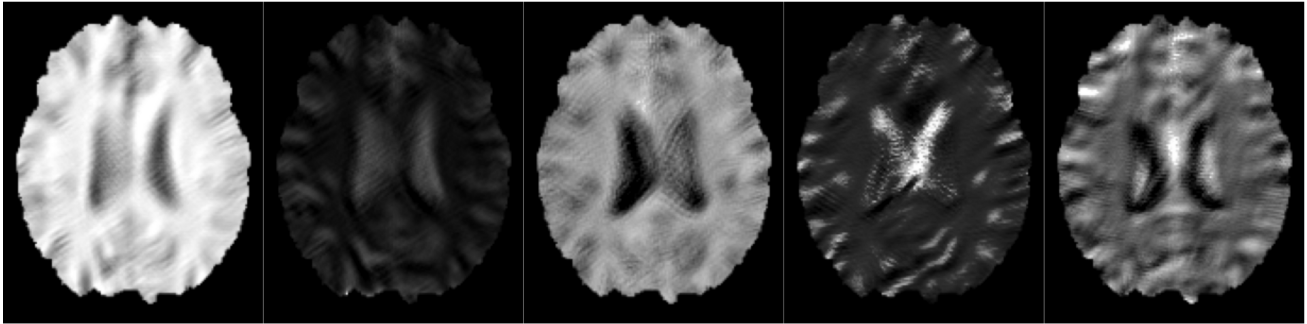


Figure S3. Axial mid-slices of augmented samples generated using the RC-based contrast augmentation method with  $3 \times 3 \times 3$  and  $5 \times 5 \times 5$  convolution kernels, resulting in visible blurring effects.

of anatomical landmark detection outcomes.

It is important to note that while the augmented scans with RC are inputs to the anatomical landmark detection model ( $f(\cdot; \theta)$ ), the calculated deformation field (Eq. 1) is applied to deform the scans before RC augmentation (Eq. 2) and the subsequent calculation of similarity and registration loss functions. This approach is based on the fact that RC does not alter the geometric properties of the scans but instead generates arbitrary contrast variations. This forces the model to predict landmarks independently of their contrasts. Consequently, this enables the use of a mono-modal loss function in Eq. 2, such as mean square error (MSE), while eliminating the need for computationally expensive metrics like mutual information (MI), normalized mutual information (NMI), or descriptors like modality independent neighborhood descriptor (MIND).

#### 4. Baselines

It is important to note that we did not include the 3D U-Net as one of our baselines for direct landmark detection because it failed to converge and performed poorly on the publicly available test sets. This outcome was expected, as 3D U-Net typically has a much heavier parameter load compared to simpler architectures like the 3D supervised

CNN we implemented. Given our limited labeled data (122 scans), the 3D U-Net struggled to converge effectively. Therefore, we opted to use a 3D CNN as the supervised learning baseline, which is more suited for scenarios with constrained datasets.